IEEE Access
Multidisciplinary | Rapid Review | Open Access Journal

Received May 12, 2021, accepted June 15, 2021, date of publication June 30, 2021, date of current version July 16, 2021.

Digital Object Identifier 10.1109/ACCESS.2021.3093704

A Transparent All-Dielectric Multifunctional Nanoantenna Emitter Compatible With Thermal Infrared and Cooling Scenarios

BAHRAM KHALICHI[1,2], (Member, IEEE), AMIR GHOBADI[1,2], ATAOLLAH KALANTARI OSGOUEI[1,3], HASAN KOCER[1], AND EKMEL OZBAY[1,2,3,4]

[1]Nanotechnology Research Center (NANOTAM), Bilkent University, 06800 Ankara, Turkey
[2]Department of Electrical and Electronics Engineering, Bilkent University, 06800 Ankara, Turkey
[3]Department of Physics, Bilkent University, 06800 Ankara, Turkey
[4]Institute of Materials Science and Nanotechnology (UNAM), Bilkent University, 06800 Ankara, Turkey

Corresponding author: Bahram Khalichi (bahram@ee.bilkent.edu.tr)

ABSTRACT In modern thermal infrared applications, multi-spectral camouflage scenarios should be developed to mitigate the thermal signature of an object. In general, camouflage needs to be satisfied in two main optical ranges: visible, and infrared (IR). In the IR range, two main camera modes are deployed to detect the IR signature of an object: *i*) short-wave IR (SWIR) cameras that detect the solar photons reflected off a surface, *ii*) mid-wave IR (MWIR) and long-wave IR (LWIR) cameras that directly collect the blackbody photons emitted from a hot object. Therefore, in an ideal scheme to acquire a multi-spectral camouflage function with self-cooling capability, the object should have: *i*) perfect absorption in the SWIR range, *ii*) perfect reflection in the MWIR and LWIR ranges, *iii*) perfect absorption and one-way transmission in non-transmissive IR (NTIR) window (to radiatively cool itself), and *iv*) visible transparency (to keep background visual appearance intact and to minimize the heat build-up due to solar absorption). In this paper, an all-dielectric nanoantenna emitter design is developed to comply with all the above-mentioned requirements. The approach relies on the indium tin oxide (ITO) grating structures coated on a flexible and transparent substrate (polystyrene). The spectral behaviors of the proposed structure are obtained using both analytical and numerical approaches. The design has an absorption peak with 0.8 amplitude in the SWIR mode (for the backward and forward illuminations), while it shows average reflections $\simeq 0.7$ in the MWIR and LWIR ranges for the forward illumination. The peak values of transmission and absorption within the NTIR window for the forward illumination are around 0.6 and 0.9, respectively. Meanwhile, the use of lossless materials within the visible range provides visible light transmission and minimizes the heat build-up due to solar absorption. In addition, the radiated power calculation model is utilized to demonstrate the low power detection on the IR cameras.

INDEX TERMS Binary grating, nanoantenna emitter/absorber, plasmonic structure, thermal infrared applications, thermal camouflage.

I. INTRODUCTION

Camouflage technology is developed to conceal the signature of an object from potential threats. However, the advancement in sensors pushed this field to multi-spectral camouflage requirements in order to cover the multiple detection scenarios [1]–[3]. In general, camouflage needs to be satisfied in two main wavelength ranges; *i*) visible and *ii*) infrared (IR). For the visible range, the use of pigments with proper coloration can provide visual camouflage via imitating the surrounding background or by resembling something else. However, for the IR case, we need to cover multiple detection ranges to mitigate the IR signature of an object without disturbing the visible appearance.

The associate editor coordinating the review of this manuscript and approving it for publication was Fulvio Schettino.

According to Planck's radiation law [4], [5], a blackbody object in thermal equilibrium with a temperature above absolute zero spontaneously and continuously emits electromagnetic radiation mainly in the IR range [4]–[7] where the spectral peak position of the emitted power density is tuned by the object's temperature (higher temperature induces a blue shift) [7], [8]. In addition, the total emissive power per unit area from a hot object can be described by the Stefan–Boltzmann law [9] as a function of both temperature and material parameter. The emissivity as a material-dependent parameter is defined to calculate the total emissive power of the corresponding object. Therefore, the obtained total emissive power is directly proportional to the fourth power of the temperature (T^4) and the surface emissivity (ε). On the other hand, the surface emissivity of the object at thermodynamic equilibrium is connected to the optical absorption of the surface as $\varepsilon(T, \lambda) = \alpha(T, \lambda)$, according to Kirchhoff's radiation law [10]. Therefore, tailoring the absorption spectral response of a design is effectively equivalent to controlling its radiation character.

The ability to control the thermal radiation of an object has attracted extensive research interests in recent years from scientific and technological points of view [1], [2], [11]–[13]. Decreasing the surface temperature and modifying the surface emissivity are two common approaches to controlling the thermal radiation of an object [13], [14]. It is of great significance if one can reduce both the infrared (IR) emittance and the temperature of the object simultaneously. However, the poor efficiency of the thermal radiation leads to an increase in the real temperature of the object [15]. Therefore, engineering or controlling the thermal radiation with wavelength-selective emitters is found to be a robust solution. Wavelength-selective emitters have potential applications in thermophotovoltaic systems, medical fields, radiative cooling, environmental monitoring, fire alarm, night vision, and IR technologies [11], [12], [16]–[46]. In addition, wavelength-selective emissive structures are extensively exploited in the IR camouflage technology to reduce the detectability of an object [17]–[22]. In general, the thermal detectors/cameras observe the IR electromagnetic waves emitted from the surfaces of targets in the two main IR atmospheric transparent windows: the mid-wave infrared (MWIR, $3 - 5\,\mu$m) and the long-wave infrared (LWIR, $8 - 12\,\mu$m) ranges. In these spectra, the majority of the thermal radiation propagates through the atmosphere with minimal absorption [11], [12]. Therefore, an efficient camouflage scenario should involve the achievement of low observability by reducing the emitted waves from the surfaces of coated targets within the atmospheric windows and allowing strong emission within an atmospheric non-transmissive window (called NTIR: non-transmissive IR range through this paper, $5 - 8\,\mu$m) for radiative cooling. Since the thermal radiation originates from top surfaces, a common approach to have a wavelength-selective IR emission is altering and modifying the optical absorption where the surfaces can be coated by photonic crystals, plasmonic metasurfaces, phase change materials, and ferroelectric materials [17]–[22], [47], [48]. Among the coating approaches, plasmonic metamaterials [49] constitute one of the most promising configurations enabling the realization of perfect absorption with wavelength selectivity. Similarly, metamaterial designs for camouflage technology have been developed for various symmetric and nonsymmetric array structures to achieve multi-functionalities, such as tunability, adaptivity, and wideband responses [48], [50]–[52]. However, most of these are metal-based designs with partial absorption/reflection characteristics in the visible range. These coatings, therefore, not only change the visual appearance of the object but can also cause heating upon irradiation by the solar spectrum. Therefore, to avoid heat build-up, the proposed design should have low solar absorption and high infrared emission and transmission in the NTIR window (while keeping its camouflage character intact).

Besides MWIR and LWIR mode cameras, another IR detection platform is based on short-wave IR (SWIR, $0.9 - 1.7\,\mu$m) thermal cameras. Unlike others, an SWIR camera does not rely on the blackbody photons of an object but rather the reflected solar photons from its surface. Therefore, to conceal the object from SWIR cameras, the surface should have an absorptive property in the SWIR range. Finally, meeting all of these necessities can provide us a comprehensive multi-spectral camouflage strategy.

In this paper, we propose an all-dielectric nanoantenna emitter to simultaneously satisfy all the above-mentioned requirements for different multi-spectral camouflage scenarios. The proposed design also acts as a visibly transparent multifunctional window by hiding indoor main targets from the thermal as well as reflected IR cameras besides cooling itself and the surrounding medium due to the realization of wavelength-selective emission and transmission spectra within the NTIR range. The spectral behaviors of the proposed nanoantenna emitter under a backward normal illumination (illumination from an outdoor environment) demonstrate an average absorption value of $\simeq 0.8$ in the SWIR mode. While it shows an average reflection intensity > 0.7 in the MWIR and LWIR ranges for a forward illumination (illumination from an indoor environment). The peak values of transmission and absorption within NTIR are around 0.6 and 0.9 for the forward illumination (illumination from the indoor environment). In addition, using a lossless visible light-transparent material provides a visible transparency property for the proposed design and minimizes the heat build-up due to solar radiation. The design is based on the visible light-transparent materials including indium tin oxide (ITO) as one-dimensional binary grating (BG) and polystyrene (PS) as a substrate where the softness of the substrate could also improve the application prospects. Finally, the power analysis model demonstrates a good camouflage performance of the design due to the combined effects of wavelength-selective emissivity (absorptivity) and transmissivity.

II. DESIGN METHODOLOGY, OPERATION PRINCIPLE, AND SIMULATION RESULTS

All of the possible detection scenarios of a hot object are schematically explained in Fig. 1(a) and the proposed BG nanoantenna emitter, consisting of ITO grating patterned on top of PS substrate, is shown in Fig. 1(b). The ITO grating is selected as an IR-responsive visible transparent antenna, while the PS substrate is used as a transparent and flexible dielectric with a near-zero extinction coefficient in our desired IR region ($1 - 12\,\mu$m). In the simulations, the ITO is considered as a dispersive medium with permittivity values experimentally extracted, as explained in our previous work [53] and the relative permittivity of PS substrate is chosen as 2.43. The geometrical parameters of each unit cell of the BG nanoantenna emitter namely the period, width, and thickness (height) are set as p, w, and t, respectively.

Broadband simulations using the rigorous coupled-wave analysis (RCWA) [54] method as an analytical approach and the commercial Lumerical finite-difference time domain (FDTD) software package as a numerical approach are performed to investigate the optical properties of the proposed nanoantenna emitter and to validate the obtained results. In these simulations, the nanoantenna emitter is extended infinitely along the x and y directions and normally illuminated by an $x-$polarized (transverse magnetic: TM$-$polarization) uniform plane-wave propagating along the $\pm z$ directions. Periodic boundary conditions are utilized to model the infinite structure in the numerical simulation domain. It should be noted that, for the proposed structure with a TM$-$polarized illumination, all of the diffracted waves lie in the x-z plane. However, such a design strategy can be easily generalized to a polarization-insensitive architecture such as a 2-D square-shaped patch which supports strong light-matter interaction for both TM and TE (transverse electric) waves. In the proposed structure, the resonance wavelengths are dependent on the periodicity (p), width (w), and thickness (t) of the grating. Accordingly, tuning, extending, and shifting of the resonances mainly rely on the rational structural design. These geometrical parameters are optimized to achieve the desired goals in the reflection, transmission, and absorption spectra by considering the fact that the wavelength-dependent surface emissivity (absorptivity) is obtained via $\varepsilon_\lambda = 1 - R_\lambda - T_\lambda$ according to Kirchhoff's law where R_λ and T_λ are the reflectivity and the transmissivity of the nanoantenna emitter as a function of wavelength (including both forward and backward illuminations). The optimization is achieved in such a way that the excited resonances in the absorption spectrum match the atmospheric absorption window (NTIR range) and the SWIR range. Moreover, to minimize the MWIR and LWIR signatures of the object, the absorption and transmission of the design should be suppressed in these ranges. In other words, the design should be as reflective as possible in the MWIR and LWIR ranges. Taking all these considerations into account, the width of the grating ridge is optimized to $w = 3.7\,\mu$m where the periodicity of the grating (p) is fixed at $4.8\,\mu$m, and the grating thickness is tuned to be $t = 1.2\,\mu$m. The spectral responses of the designed nanoantenna emitter are plotted in Fig. 1(c) and Fig. 1(d) for the forward ($-z$) and backward ($+z$) illuminations, respectively, between $0.9\,\mu$m and $12\,\mu$m. To have a better comparison, the atmosphere absorptivity spectrum, modeled by considering the US standard atmosphere compositions at the vertical distance of 5 km [55], is also plotted with the light blue area in Fig. 1(c) and Fig. 1(d). It is observed that the analytical and numerical approaches are in good agreement with each other.

The operation of this nanoantenna emitter should be evaluated from two perspectives: *i*) forward illumination which is the direction from a hot object to the IR cameras and *ii*) backward illumination which is from the IR cameras to the object. In summary, for the forward illumination, the coating should be: *i*) reflective in the MWIR and LWIR ranges and *ii*) transmissive/emissive throughout the NTIR range. As depicted in Fig. 1(c), the optical spectrum under the forward incidence shows dominant reflective behavior in the MWIR and LWIR ranges while exhibiting a distinct narrowband absorption resonance at $\lambda_1^{\text{abs}} = 7.50\,\mu$m. Meanwhile, the design has a transmissive character in the NTIR range with a resonance located at $\lambda_1^{\text{trans}} = 7.36\,\mu$m. From these results, the proposed spectrally-selective nanoantenna emitter radiatively cools the coated object down while concealing it from the MWIR and LWIR detectors. On the other side, for the backward illumination scenario, the antenna should act as: *i*) absorptive coater in the SWIR range and *ii*) reflective coater in the MWIR and LWIR ranges. As seen from Fig. 1(d), the absorption spectrum shows a narrow resonance located at $\lambda_1'^{\text{abs}} = 1.30\,\mu$m, covering the SWIR range. Considering the lossless nature of both ITO and PS in the visible range, the design has also high transparency and low solar absorptivity in this range for both directions. A better quantitative comparison can be acquired by calculating the averaged T_λ, R_λ, and ε_λ values for both directions in different IR ranges as depicted in Fig. 1(e) and Fig. 1(f). According to the results, the design is highly reflective in the MWIR and LWIR ranges and highly absorptive in the SWIR range under both-side illuminations.

The physical origin of the resonant transmission and absorption behaviors of the nanoantenna emitter is analyzed for the forward illumination to determine the types of supported modes by the structure. To achieve that, the corresponding total electric and magnetic fields on the x-z plane together with the absorbed (dissipated) power density and the Poynting vector distribution are shown in Fig. 2. At the resonance wavelength of λ_1^{trans} (also see Fig. 1(c), the zoomed part), the electric field distribution is strongly enhanced and confined within the groove and it experiences a large discontinuity with much higher amplitude in the low-index side (groove) for satisfying the continuity of the normal component of the electric flux density. This means that the electric field distribution within the groove represents a slot-waveguide like behavior [56] [as it can be seen from

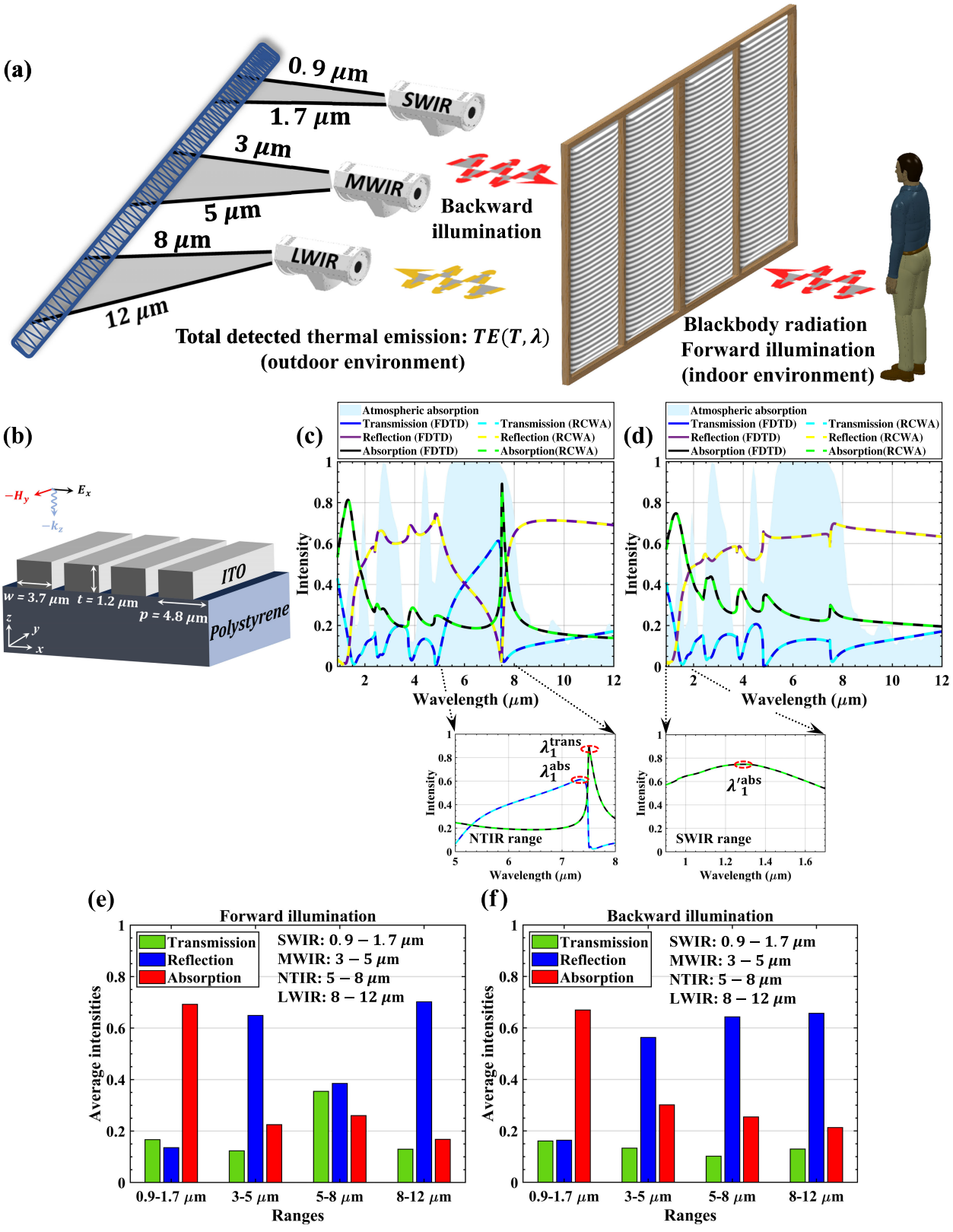

FIGURE 1. (a) All of the possible detection scenarios of a hot object. (b) Schematic representation of the proposed nanoantenna emitter. (c) Forward and (d) backward illumination spectra calculated by numerical and analytical approaches for the proposed structure when the object is illuminated by an $x-$polarized uniform plane wave propagating along the $-z$ and $+z$ directions, respectively. The calculated average intensities for the (e) forward and (f) backward illuminations obtained via integration of the spectral parameters of the nanoantenna emitter with respect to wavelength at different ranges including SWIR, MWIR, NTIR, and LWIR.

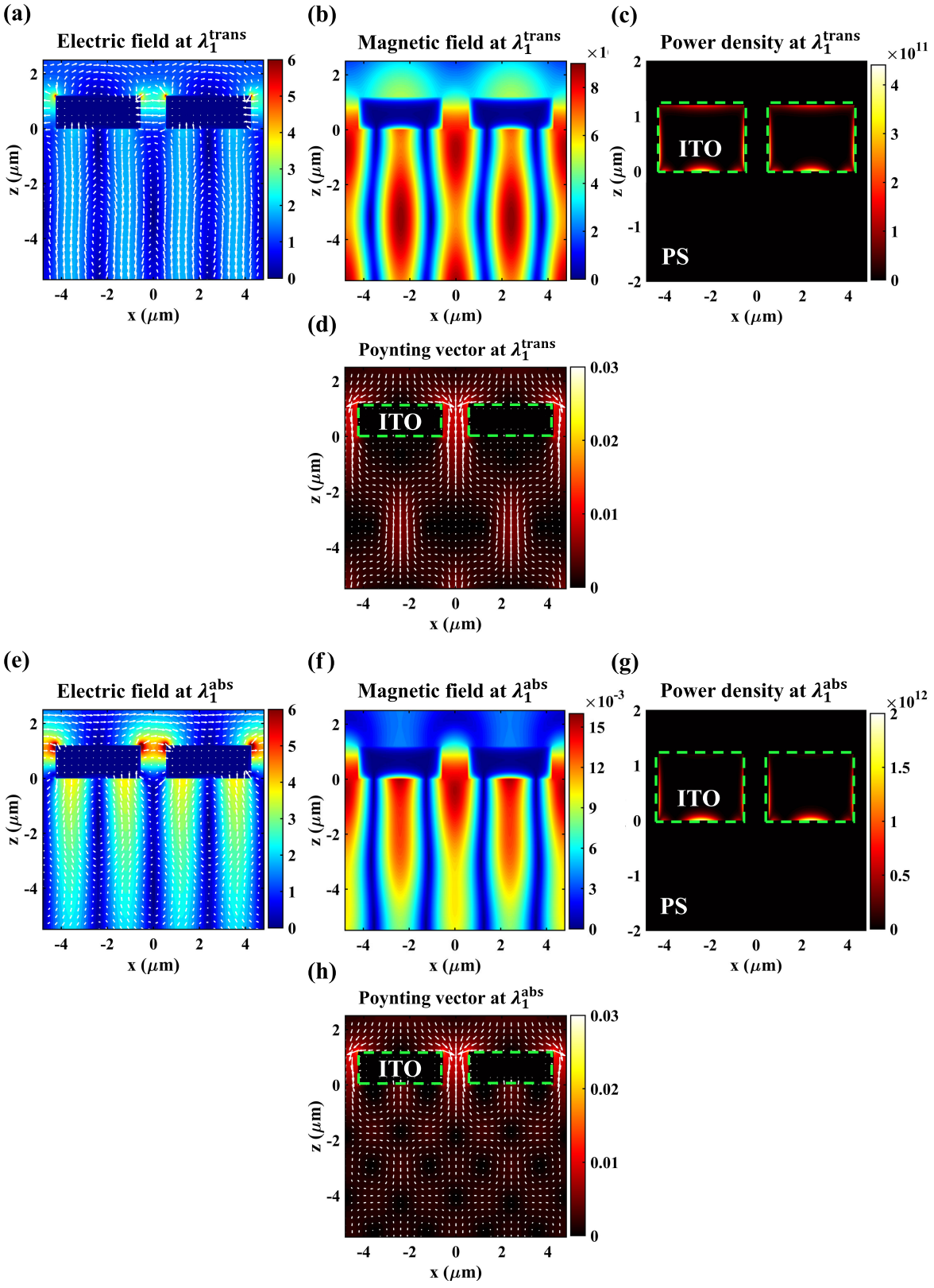

FIGURE 2. (a) Absolute value and vector field distribution (real part) of the total electric field, (b) absolute value of the total ($y-$directed) magnetic field, (c) the absorbed (dissipated) power density, and (d) the Poynting vector distribution of the proposed nanoantenna emitter on the x-z plane obtained for a two-unit cell at the resonance wavelength of λ_1^{trans} (belonging to the transmission spectrum) when the structure is normally illuminated by an $x-$polarized uniform plane wave propagating along the $-z$ direction. (e)-(h) The same distributions at the resonance wavelength of λ_1^{abs} belonging to the absorption spectrum. The dashed green lines represent the ITO-based grating areas.

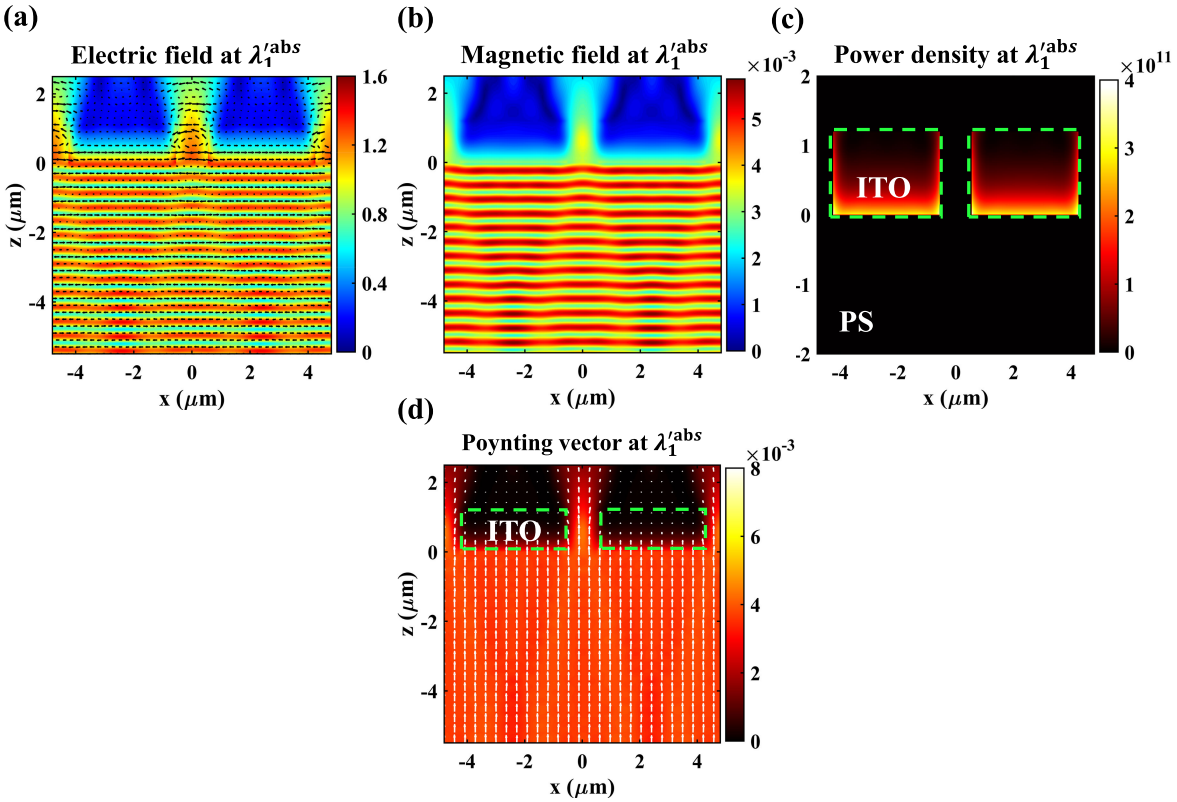

FIGURE 3. (a) Absolute value and vector field distribution (real part) of the total electric field, (b) absolute value of the total ($y-$directed) magnetic field, (c) the absorbed (dissipated) power density, and (d) the Poynting vector distribution of the proposed nanoantenna emitter on the x-z plane obtained for a two-unit cell at the resonance wavelength of $\lambda_1'^{abs}$ when the structure is normally illuminated by an $x-$polarized uniform plane wave propagating along the $+z$ direction. The dashed green lines represent the ITO-based grating areas.

the electric and magnetic field distributions given in Fig. 2(a) and Fig. 2(b)], which causes an average transmission of 40% through the groove. Meanwhile, the slots corresponding to the grating behave as a 1-D cavity forced to resonate under vertical Fabry-Perot conditions when the frequency is close to the cavity resonance. Therefore, the transmission peak at the wavelength of λ_1^{trans} is due to the dominancy of the slot-waveguide like behavior mode that results in the field enhancement inside the groove, and owing to its non-evanescent nature, allows transmission through the grating to the next environment at the resonant wavelength of the cavity (see electric field and Poynting vector distributions presented in Fig. 2(a) and Fig. 2(d), respectively). In addition, the diffraction of electric field results in satisfying the phase-matching condition and the excitation of surface plasmons (SPs) at the upper and lower interfaces of ITO grating as seen from the electric field and the absorbed power distributions given in Fig. 2(a) and Fig. 2(c), respectively. Therefore, a partial amount of incident power belonging to the hot object is absorbed by the nanoantenna emitter within the NTIR range as seen from Fig. 1(c) and Fig. 1(e).

Similarly, at the absorption resonance wavelength of λ_1^{abs} (see Fig. 1(c), the zoomed part), the excitation of SPs is responsible for the light perfect absorption. This can be observed by investigating the total electric and magnetic field distributions together with the absorbed (dissipated) power density and the Poynting vector distribution given in Fig. 2(e) to Fig. 2(h). Furthermore, the circulating electric field within the groove together with the $y-$directed magnetic field distribution attributed to the fact that the second resonance (λ_1^{abs}) is originated from the concept of magnetic dipole excitation which is in contrast with the slot-waveguide like behavior of the former resonance (λ_1^{trans}). At this resonance, most of the incident electric field is coupled to the magnetic dipole resonance within the groove and SP resonance as clearly seen from the vector electric field and absorbed power distributions given in Fig. 2(e) and Fig. 2(g), respectively. Meanwhile, the excitation of SPs has the main responsibility for the absorption of the incident power (90%, inside the atmospheric window: NTIR range) at the interfaces of the ITO-based grating and the dielectric substrate as shown in Fig. 2(g).

The physical behavior of the nanoantenna emitter under the backward incidence at the resonance wavelength of $\lambda_1'^{abs}$ corresponding to the SWIR mode spectrum is also analyzed (see Fig. 1(d), the zoomed part). In this scenario, a broadband light normally hits the metal grating from the outdoor environment [see Fig. 1(a)] where the circulating electric

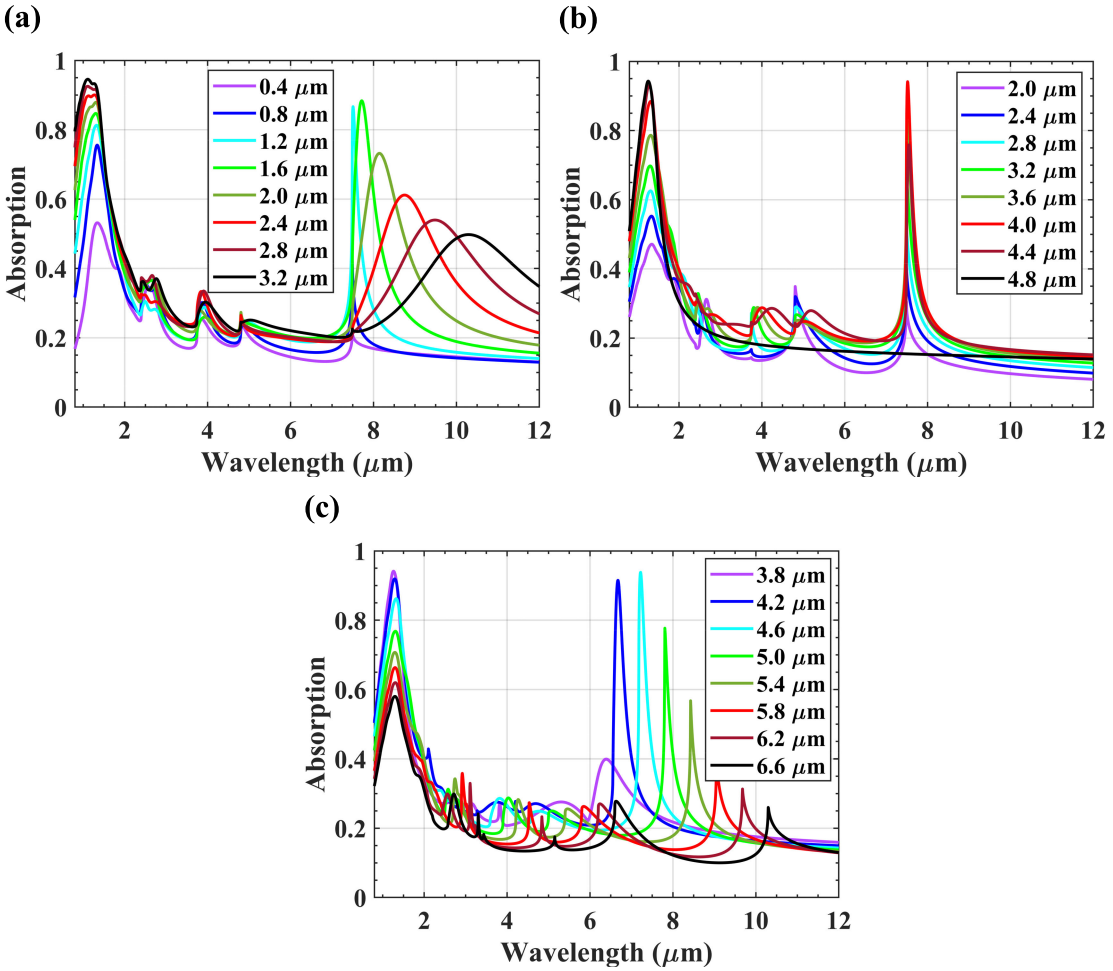

FIGURE 4. Dependency of the absorption spectrum of the proposed BG nanoantenna emitter on the variation of the geometrical parameters, including: (a) the thickness [$0.4 < t < 3.2$ when $w = 3.7$, and $p = 4.8$] (b) the width [$2 < w < 4.8$ when $t = 1.2$, and $p = 4.8$] and (c) the periodicity [$3.8 < p < 6.6$ when $t = 1.2$, and $w = 3.7$] of the grating when the structure is normally illuminated by an $x-$polarized uniform plane wave propagating along the $-z$ direction.

field is confined within the groove as can be observed from Fig. 3(a). The circulating electric field within the groove together with the $y-$directed magnetic field distribution [Fig. 3(b)] demonstrate that the excited resonance ($\lambda_1^{'abs}$) is due to the excitation of magnetic dipoles. As presented in Fig. 3(c) and Fig. 3(d), the light confinement leads to the dissipation of the incident power within the lossy metallic ITO grating (80% absorption) while a partial amount of the incident power can be transmitted to the next environment (20%).

Tuning, extending, and shifting of the resonances are mainly defined by the application requirements. Therefore, the impact of different geometrical parameters of the BG nanoantenna emitter on the optical performances needs to be scrutinized. Figures 4(a) to 4(c) represent the absorption spectra as a function of wavelength for different geometrical parameters including the thickness, width, and periodicity of the grating. The impact of each geometrical parameter is investigated by sweeping its value while the other parameters of the grating are kept at their optimal values as given in Fig. 1(b). It is observed that increasing the thickness and periodicity of the grating result in red-shift and suppression of the absorption peaks [see Fig. 4(a) and Fig. 4(c)], while the variation of the width dominantly modulates the amplitude without imposing spectral shift as seen from Fig. 4(b). According to Fig. 2(e), the excitation of the magnetic dipoles within the groove as well as their extension and coupling to the SPs at the vicinity of the groove are the main reasons for the most amount of the absorption in the structure. Therefore, it can be concluded that increasing the thickness of the grating can result in the non-efficient excitation of the magnetic dipoles and their extension to the edges, and the excitation of the SPs at longer wavelengths with lower absorption intensities. However, the variation of the width (filling factor: $f = \frac{w}{p}$, $0.4 < f < 1$) only decreases the amount of the absorption at the almost fixed resonance wavelength since the overall dimension of the unit cell is fixed. Contrarily, the variation of the periodicity ($0.55 < f < 1$) causes the excitation of the magnetic dipoles and SPs at longer wavelengths due to an increase in the overall dimension of the unit cell.

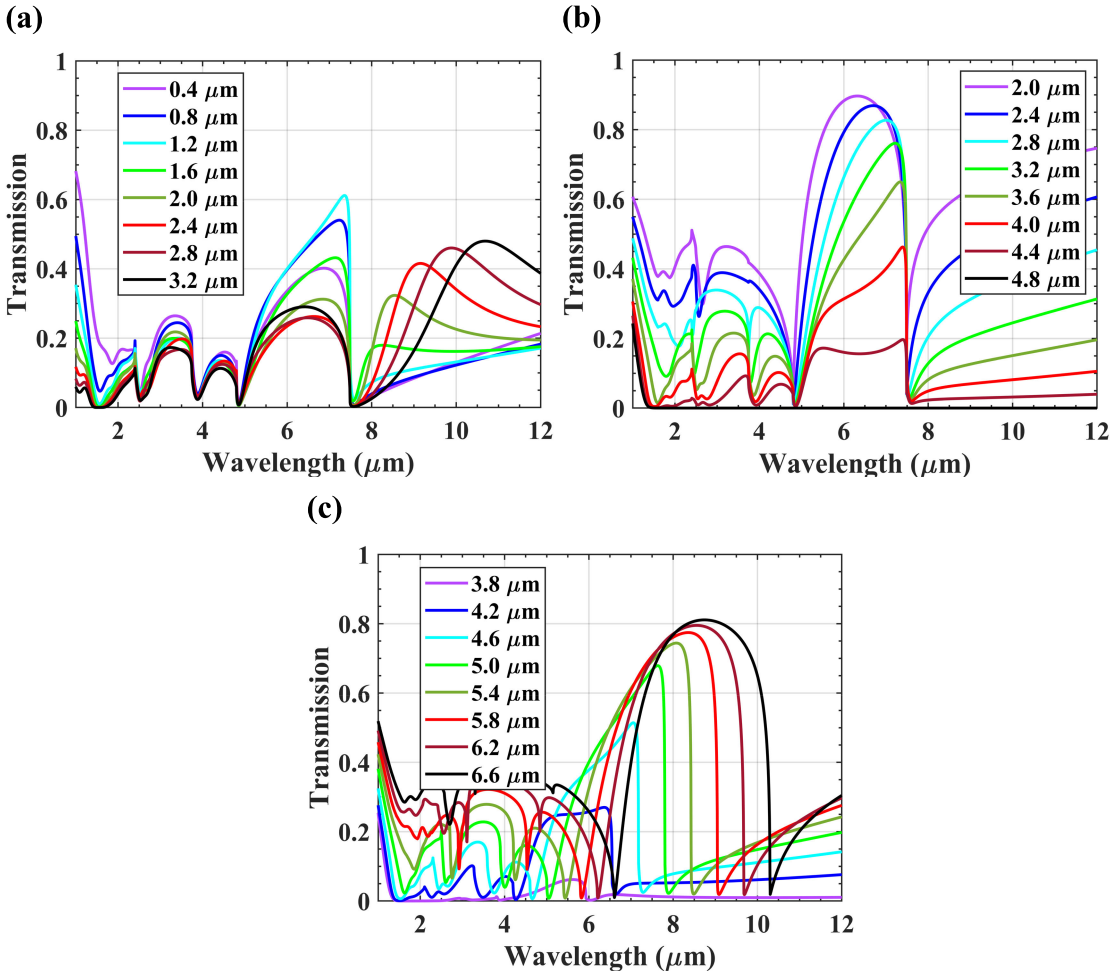

FIGURE 5. Dependency of the transmission spectrum of the proposed BG nanoantenna emitter on the variation of the geometrical parameters, including: (a) the thickness [$0.4 < t < 3.2$ when $w = 3.7$, and $p = 4.8$] (b) the width [$2 < w < 4.8$ when $t = 1.2$, and $p = 4.8$] and (c) the periodicity [$3.8 < p < 6.6$ when $t = 1.2$, and $w = 3.7$] of the grating when the structure is normally illuminated by an $x-$polarized uniform plane wave propagating along the $-z$ direction.

This also reduces the amount of absorption due to the less efficient extension and coupling among the magnetic dipoles and SPs. Therefore, the locations of the existing resonance wavelengths in the absorption spectrum are highly dependent on the variation of the thickness and the periodicity of the grating while all parameters affect the absorption intensities.

Similar analyses for the impact of the geometrical parameters on the resonance wavelength (λ_1^{trans}) of the transmission spectrum are conducted, as shown in Fig. 5(a) to Fig. 5(c). The transmission spectra with different grating thicknesses are shown in Fig. 5(a). With the increase of the grating thickness from 0.4 μm to 3.2 μm, the intensity at the resonance wavelength λ_1^{trans} first increases and experiences red-shift and reaches its maximum value around 0.6, then starts decreasing and experiencing blue-shift. Meanwhile, another resonance appears at longer wavelengths by increasing the thickness. From Fig. 5(b), it is clear that increasing the width of the grating from 2 μm to 4.8 μm leads to a reduction in the amount of power passed through the slots to reach the next environment. Therefore, according to the previously explained slot-waveguide like behavior of the groove [see Fig. 2(a) and Fig. 2(b)], the resonance wavelength and the amount of transmission are completely dependent on the dimensions of the groove. As seen from Fig. 5(c), by increasing the periodicity from 3.8 μm to 6.6 μm ($0.55 < f < 1$) while the width and the thickness of the grating are kept at their optimal values, the resonance wavelength red-shifts together with an improvement in the amount of its intensity.

III. POWER ANALYSIS AND THERMAL CAMOUFLAGE SCENARIO

Based on the obtained results, the proposed multifunctional nanoantenna emitter can elegantly cool itself and manage the thermal radiation of hot objects in the indoor environment [see Fig. 1(a)]. These properties can be achieved since the resonance wavelengths are adapted to be placed in the main atmospheric absorption window (NTIR range). To verify these capabilities [57], the emitted power from the indoor blackbody is calculated using thermal emission modeling as

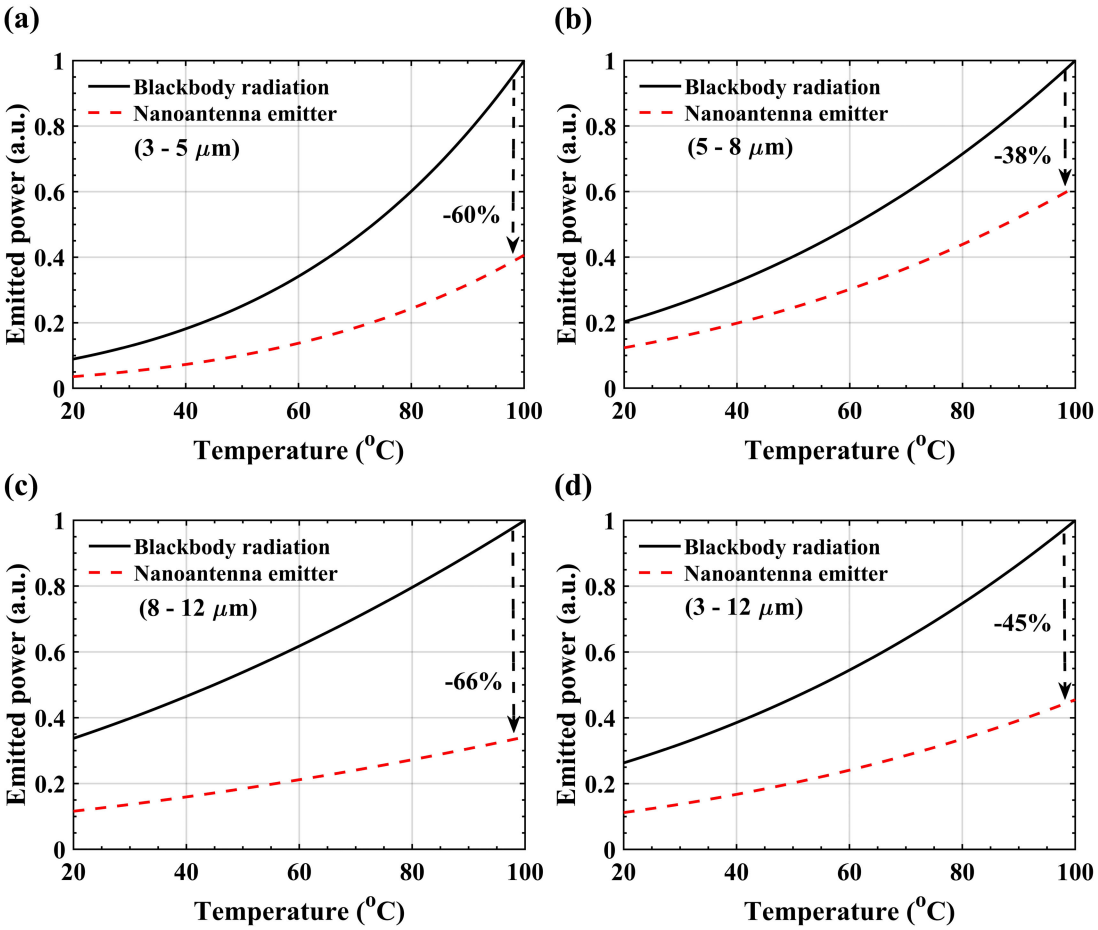

FIGURE 6. (a) Detected emitted power versus temperature at different intervals including (a) $3-5\,\mu$m, (b) $5-8\,\mu$m, (c) $8-12\,\mu$m, (d) $3-12\,\mu$m. The calculations are performed without considering the effect of the atmospheric absorption spectrum.

shown in Fig. 1(a). First, the absorptivity of the nanoantenna emitter is considered under the backward illumination for the calculation of its surface emissivity at thermodynamic equilibrium according to Kirchhoff's radiation law. Therefore, the surface emissivity of the nanoantenna emitter originated from the backward illumination can be written as:

$$\varepsilon_{\text{backward}}(\lambda) = 1 - T_{\text{backward}}(\lambda) - R_{\text{backward}}(\lambda), \quad (1)$$

where $\varepsilon_{\text{backward}}(\lambda)$, $T_{\text{backward}}(\lambda)$, and $R_{\text{backward}}(\lambda)$ are the backward absorptivity, transmissivity, and reflectivity of the proposed structure, respectively, dependent on the operating wavelength (λ). Then, Plank's law is utilized to compute the spectral radiance emitted by a blackbody object in thermal equilibrium as follows

$$BB(T,\lambda) = \frac{2\pi hc^2}{\lambda^5}\left(e^{\frac{hc}{\lambda k_B T}} - 1\right)^{-1}, \quad (2)$$

where h, c, and k_B are the Planck constant, the speed of light in vacuum, and the Boltzmann's constant, respectively. In addition, T denotes the absolute temperature of the body. Finally, the total thermal emission ($TE(T,\lambda)$) of a blackbody radiator at the indoor environment passing through the nanoantenna emitter can be obtained by

$$TE(T,\lambda) = BB(T,\lambda) \times T_{\text{forward}}(\lambda) + BB(T,\lambda) \times \varepsilon_{\text{backward}}(\lambda). \quad (3)$$

Taking an integral of (3) with respect to the wavelength over the region of interest will give the detected optical power density by IR cameras as a function of temperature. Therefore, we have

$$P = \int_{\lambda_1}^{\lambda_2} TE(T,\lambda)\, d\lambda. \quad (4)$$

In this work, the wavelength intervals are chosen as $3-5\,\mu$m, $5-8\,\mu$m, and $8-12\,\mu$m according to the atmospheric absorption and transmission windows over the $3-12\,\mu$m. The calculated detected powers using (4) for the proposed multifunctional window (nanoantenna emitter) are shown in Fig. 6(a) to Fig. 6(d) *without considering the effect of the atmospheric absorption spectrum*. The interval $5-8\,\mu$m is the region of interest that the power emission and transmission should be high enough to release the energy from the

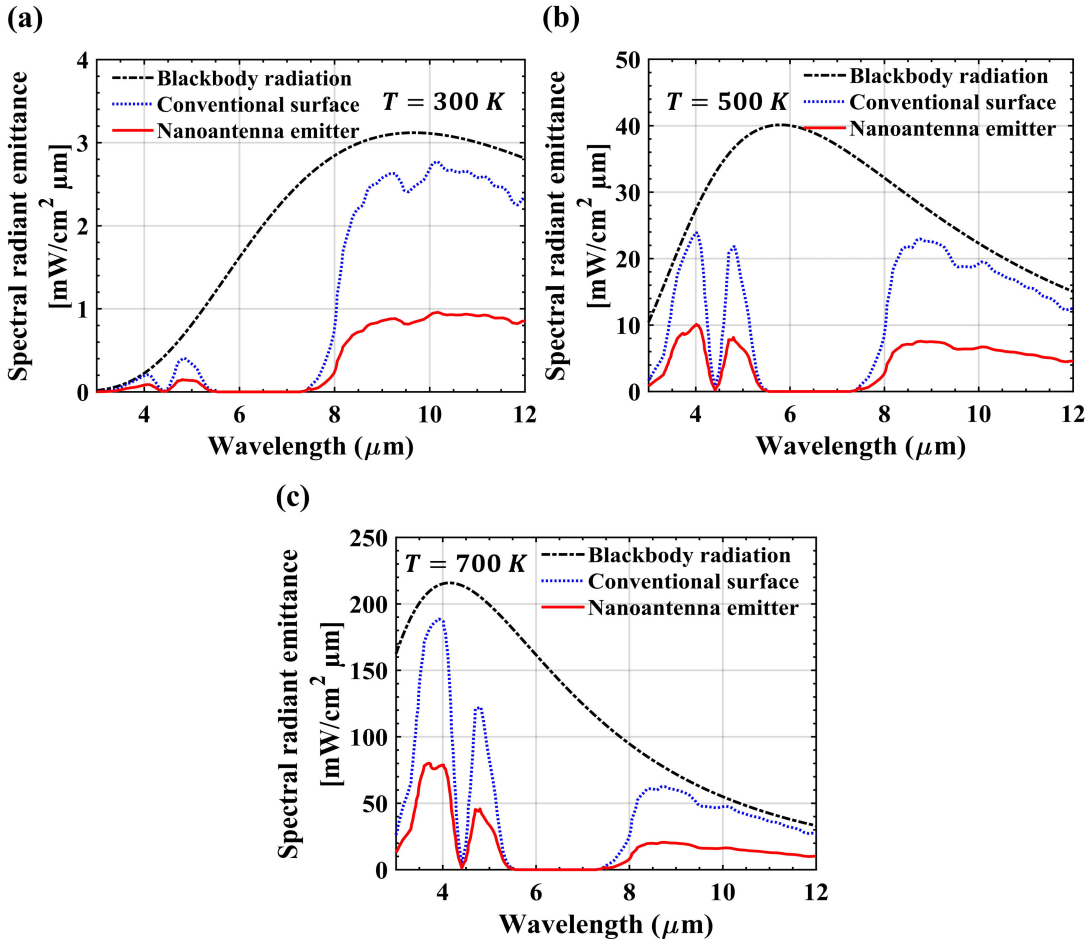

FIGURE 7. IR signatures of a blackbody, a conventional surface, and the selective nanoantenna emitter at different temperatures (a) $T = 300\,K$, (b) $T = 500\,K$, and (c) $T = 700\,K$ obtained by considering the effect of the atmospheric absorption spectrum.

indoor environment to the outside. In this region, the released power is expected to be as close as possible to the blackbody radiation so that the built-up energy can be released without causing any risk of detection by thermal cameras. Contrarily, the rest of the intervals are the ones (MWIR: $3-5\,\mu$m and LWIR: $8-12\,\mu$m) that the atmospheric windows let the emission of power. Therefore, any power releasing from indoor to outdoor environments in those regions should be as small as possible. This means that the detected power should be as far as possible from the blackbody radiation in the atmospheric windows as seen from Fig. 6(a) and Fig. 6(c).

To evaluate the performance of the proposed design, we calculate the spectral radiant emittance of *i*) a blackbody, *ii*) a conventional surface, and *iii*) the selective nanoantenna emitter at different temperatures. The IR signatures of the conventional surface $[BB(T,\lambda) \times (1-\varepsilon_{\text{atmosphere}}(T,\lambda))]$ and the selective nanoantenna emitter $[NE(T,\lambda) = TE(T,\lambda) \times (1-\varepsilon_{\text{atmosphere}}(T,\lambda))]$ can be obtained from the data of the atmospheric absorption and the calculated thermal emission of the whole indoor environment passing through the multifunctional window. Figure 7(a) compares the calculated IR signatures of the conventional surface and the selective nanoantenna emitter over the spectral radiant emittance of the blackbody radiation at room temperature ($300\,K$) by considering the radiation energy emitted from the normal direction. The IR signatures of the selective nanoantenna emitter at room temperature in the MWIR and LWIR ranges are reduced by 83.19% and 72.32% compared to the blackbody radiation, respectively. While the selective nanoantenna emitter can reduce the radiant energy by 79.84% throughout the entire wavelength band. As the temperature increases to $500\,K$ and $700\,K$, as shown in Fig. 7(b) and Fig. 7(c), respectively, the reduction rates of the IR signatures for the selective nanoantenna emitter in the MWIR and LWIR ranges are still higher than 73%. Notably, the reduction rate of the selective nanoantenna emitter is greater than 79% across a wide temperature varying from room temperature to $700\,K$ for the entire wavelength range. Therefore, it is concluded that the selective emitter can effectively suppress the thermal radiation from the indoor environment within the atmospheric windows and enhance the thermal radiation in the NTIR range ($5-8\,\mu$m) from room

TABLE 1. The reduction rates of the selective nanoantenna emitter calculated via (5).

	$3-5\,\mu$m	$8-12\,\mu$m	$3-12\,\mu$m
$T=300\,K$	83.19%	72.32%	79.84%
$T=500\,K$	80.72%	73.86%	88.97%
$T=700\,K$	78.84%	74.53%	86.53%

temperature up to $700\,K$. These also provide the cooling and invisibility of hot objects located in the indoor environment. The reduction rates of the selective nanoantenna emitter in the wavelength ranges of $3-5\,\mu$m, $8-12\,\mu$m, and the entire band for different temperatures are listed in Table 1, which are calculated using

$$\text{Reduction rate} = \sqrt{\frac{\sum_{i=1}^{n} |BB(T,\lambda_i) - NE(T,\lambda_i)|^2}{\sum_{i=1}^{n} |BB(T,\lambda_i)|^2}}, \quad (5)$$

where $i = 1, 2, \ldots, n$ denotes the number of discretization points within the region of interest.

IV. CONCLUSION

In conclusion, we proposed a wavelength-selective thermal nanoantenna emitter based on a simple BG design. The structure acts as a multifunctional window with thermal camouflage and cooling properties. In other words, the proposed design satisfies the requirements of *i*) having absorption in the SWIR range, *ii*) reflection in the MWIR and LWIR ranges, *iii*) absorption and one-way transmission in the NTIR range, and iv) visible transparency to minimize the heat build-up due to solar absorption. The performance of the proposed structure is studied and validated using numerical and analytical approaches. The suppression of total emitted thermal power without considering the atmospheric absorption spectrum is verified by calculating the detected power by IR cameras over the MWIR and LWIR ranges where 60% and 66% reductions are obtained at 100 ° C in comparison with the blackbody radiation, respectively. This calculated value increases to 38% within the NTIR range which is equivalent to the cooling of the indoor environment. Furthermore, the calculated spectral radiant emittances by considering the effect of atmospheric absorption spectrum demonstrate that the selective nanoantenna emitter can reduce the blackbody radiation energy for the whole wavelength spectrum at least by 79.84%, ranging from room temperature to $700\,K$ which also reveal the superiority of the proposed design for being utilized in thermal camouflage applications.

DISCLOSURES

The authors declare no conflict of interest.

REFERENCES

[1] O. Salihoglu, H. B. Uzlu, O. Yakar, S. Aas, O. Balci, N. Kakenov, S. Balci, S. Olcum, S. Süzer, and C. Kocabas, "Graphene-based adaptive thermal camouflage," *Nano Lett.*, vol. 18, no. 7, pp. 4541–4548, Jul. 2018.
[2] M. Li, D. Liu, H. Cheng, L. Peng, and M. Zu, "Manipulating metals for adaptive thermal camouflage," *Sci. Adv.*, vol. 6, no. 22, pp. 1–11, 2020.
[3] E. Buhara, A. Ghobadi, B. Khalichi, H. Kocer, and E. Ozbay, "Mid-infrared adaptive thermal camouflage using a phase-change material coupled dielectric nanoantenna," *J. Phys. D, Appl. Phys.*, vol. 54, no. 26, pp. 1–11, 2021.
[4] M. Planck, "On the law of the energy distribution in the normal spectrum," *Ann. Phys*, vol. 4, no. 553, pp. 1–11, 1901.
[5] M. Planck, "Über das gesetz der energieverteilung im normalspektrum," in *Von Kirchhoff bis Planck* (Reihe Wissenschaft), H. G. Schöpf, Ed. Wiesbaden, Germany: Springer, 1978, pp. 178–191.
[6] M. Planck, "On the law of distribution of energy in the normal spectrum," *Annalen der physik*, vol. 4, no. 553, p. 1, 1901.
[7] M. Planck, *The Theory of Heat Radiation*. Chelmsford, MA, USA: Courier Corporation, 2013.
[8] R. Karwa, "Mass transfer," in *Heat and Mass Transfer*. Singapore: Springer, 2020.
[9] J. Stefan, "Über die Beziehung zwischen der Wärmestrahlung und der Temperatur," in *Sitzungsberichte der Mathematisch-naturwissenschaftlichen Classe der Kaiserlichen Akademie der Wissenschaften* (Proceedings of the Imperial Philosophical Academy), vol. 79. Vienna, Austria: Mathematical and Scientific Class, (in German), 1879, pp. 391–428.
[10] G. Kirchhoff, "Über das verhältnis zwischen dem emissionsvermögen und dem absorptionsvermögen der körper für wärme und licht," in *Von Kirchhoff bis Planck* (Reihe Wissenschaft), H. G. Schöpf, Ed. Wiesbaden, Germany: Springer, 1978, pp. 131–151.
[11] D. Zhao, A. Aili, Y. Zhai, S. Xu, G. Tan, X. Yin, and R. Yang, "Radiative sky cooling: Fundamental principles, materials, and applications," *Appl. Phys. Rev.*, vol. 6, no. 2, Jun. 2019, Art. no. 021306.
[12] X. Sun, Y. Sun, Z. Zhou, M. A. Alam, and P. Bermel, "Radiative sky cooling: Fundamental physics, materials, structures, and applications," *Nanophotonics*, vol. 6, no. 5, pp. 997–1015, Jul. 2017.
[13] H. Zhu, Q. Li, C. Zheng, Y. Hong, Z. Xu, H. Wang, W. Shen, S. Kaur, P. Ghosh, and M. Qiu, "High-temperature infrared camouflage with efficient thermal management," *Light, Sci. Appl.*, vol. 9, no. 1, pp. 1–8, Dec. 2020.
[14] M. Pan, Y. Huang, Q. Li, H. Luo, H. Zhu, S. Kaur, and M. Qiu, "Multi-band middle-infrared-compatible camouflage with thermal management via simple photonic structures," *Nano Energy*, vol. 69, pp. 1–9, Mar. 2020.
[15] T. Kim, J.-Y. Bae, N. Lee, and H. H. Cho, "Hierarchical metamaterials for multispectral camouflage of infrared and microwaves," *Adv. Funct. Mater.*, vol. 29, no. 10, pp. 1–8, 2019.
[16] R. Usamentiaga, P. Venegas, J. Guerediaga, L. Vega, J. Molleda, and F. Bulnes, "Infrared thermography for temperature measurement and non-destructive testing," *Sensors*, vol. 14, no. 7, pp. 12305–12348, Jul. 2014.
[17] L. Xiao, H. Ma, J. Liu, W. Zhao, Y. Jia, Q. Zhao, K. Liu, Y. Wu, Y. Wei, S. Fan, and K. Jiang, "Fast adaptive thermal camouflage based on flexible VO_2/graphene/CNT thin films," *Nano Lett.*, vol. 15, no. 12, pp. 8365–8370, 2015.
[18] T. Z. Yang, Y. Su, W. Xu, and X. D. Yang, "Transient thermal camouflage and heat signature control," *Appl. Phys. Lett.*, vol. 109, no. 12, 2016, Art. no. 121905.
[19] Y. Qu, Q. Li, L. Cai, M. Pan, P. Ghosh, K. Du, and M. Qiu, "Thermal camouflage based on the phase-changing material GST," *Light, Sci. Appl.*, vol. 7, no. 1, pp. 1–10, Dec. 2018.
[20] N. Lee, T. Kim, J.-S. Lim, I. Chang, and H. H. Cho, "Metamaterial-selective emitter for maximizing infrared camouflage performance with energy dissipation," *ACS Appl. Mater. Interfaces*, vol. 11, no. 23, pp. 21250–21257, Jun. 2019.
[21] H. Ji, D. Liu, H. Cheng, C. Zhang, and L. Yang, "Vanadium dioxide nanopowders with tunable emissivity for adaptive infrared camouflage in both thermal atmospheric Windows," *Sol. Energy Mater. Sol. Cells*, vol. 175, pp. 96–101, Feb. 2018.
[22] S. Hong, S. Shin, and R. Chen, "An adaptive and wearable thermal camouflage device," *Adv. Funct. Mater.*, vol. 30, no. 11, pp. 1–7, 2020.
[23] H. Bao, C. Yan, B. Wang, X. Fang, C. Y. Zhao, and X. Ruan, "Double-layer nanoparticle-based coatings for efficient terrestrial radiative cooling," *Sol. Energy Mater. Sol. Cells*, vol. 168, pp. 78–84, Aug. 2017.
[24] L. Zhao, H. Liu, Z. He, and S. Dong, "All-metal frequency-selective absorber/emitter for laser stealth and infrared stealth," *Appl. Opt.*, vol. 57, no. 8, pp. 1757–1764, 2018.

[25] Y. Shen, Y.-Q. Pang, J.-F. Wang, H. Ma, Z.-B. Pei, and S.-B. Qu, "Ultra-broadband terahertz absorption by uniaxial anisotropic nanowire metamaterials," *IEEE Photon. Technol. Lett.*, vol. 27, no. 21, pp. 2284–2287, Nov. 1, 2015.

[26] X. Yin, L. Chen, and X. Li, "Ultra-broadband super light absorber based on multi-sized tapered hyperbolic metamaterial waveguide arrays," *J. Lightw. Technol.*, vol. 33, no. 17, pp. 3704–3710, Sep. 1, 2015.

[27] K. Du, Q. Li, W. Zhang, Y. Yang, and M. Qiu, "Wavelength and thermal distribution selectable microbolometers based on metamaterial absorbers," *IEEE Photon. J.*, vol. 7, no. 3, pp. 1–8, Jun. 2015.

[28] C. Wu, B. Neuner, J. John, A. Milder, B. Zollars, S. Savoy, and G. Shvets, "Metamaterial-based integrated plasmonic absorber/emitter for solar thermo-photovoltaic systems," *J. Opt.*, vol. 14, no. 2, pp. 1–7, 2012.

[29] Y. K. Zhong, S. M. Fu, N. P. Ju, M.-H. Tu, B.-R. Chen, and A. Lin, "Fully planarized perfect metamaterial absorbers with NO photonic nanostructures," *IEEE Photon. J.*, vol. 8, no. 1, pp. 1–9, Feb. 2016.

[30] S. M. Fu, Y. K. Zhong, N. P. Ju, M.-H. Tu, B.-R. Chen, and A. Lin, "Broadband polarization-insensitive metamaterial perfect absorbers using topology optimization," *IEEE Photon. J.*, vol. 8, no. 5, pp. 1–11, Oct. 2016.

[31] J. Duan, R. Liu, H. Xu, R. Zhang, B. Zhang, and B.-S. Kim, "EMT conversion of composite broadband absorbent metamaterials for stealth application over X-bands," *IEEE Access*, vol. 8, pp. 153787–153798, 2020.

[32] A. K. Osgouei, H. Hajian, B. Khalichi, A. E. Serebryannikov, A. Ghobadi, and E. Ozbay, "Active tuning from narrowband to broadband absorbers using a sub-wavelength VO_2 embedded layer," *Plasmonics*, vol. 16, pp. 1013–1021, Feb. 2021.

[33] J.-Y. Jung, J. Lee, D.-G. Choi, J.-H. Choi, J.-H. Jeong, E.-S. Lee, and D. P. Neikirk, "Wavelength-selective infrared metasurface absorber for multispectral thermal detection," *IEEE Photon. J.*, vol. 7, no. 6, pp. 1–10, Dec. 2015.

[34] S. Mahmud, S. S. Islam, A. F. Almutairi, and M. T. Islam, "A wide incident angle, ultrathin, polarization-insensitive metamaterial absorber for optical wavelength applications," *IEEE Access*, vol. 8, pp. 129525–129541, 2020.

[35] D. Li, S. Lin, F. Hu, Z. Chen, W. Zhang, and J. Han, "Metamaterial terahertz sensor for measuring thermal-induced denaturation temperature of insulin," *IEEE Sensors J.*, vol. 20, no. 4, pp. 1821–1828, Feb. 2020.

[36] Y. Guo and Z. Jacob, "Thermal hyperbolic metamaterials," *Opt. Exp.*, vol. 21, no. 12, pp. 15014–15019, 2013.

[37] A. Ghanekar, L. Lin, and Y. Zheng, "Novel and efficient Mie-metamaterial thermal emitter for thermophotovoltaic systems," *Opt. Exp.*, vol. 24, no. 10, pp. A868–A877, 2016.

[38] A. K. Osgouei, H. Hajian, A. E. Serebryannikov, and E. Ozbay, "Hybrid indium tin oxide-Au metamaterial as a multiband bi-functional light absorber in the visible and near-infrared ranges," *J. Phys. D, Appl. Phys.*, vol. 54, no. 27, pp. 1–9, 2021.

[39] F. Alves, D. Grbovic, B. Kearney, N. V. Lavrik, and G. Karunasiri, "Bi-material terahertz sensors using metamaterial structures," *Opt. Exp.*, vol. 21, no. 11, pp. 13256–13271, 2013.

[40] J. A. Montoya, Z. B. Tian, S. Krishna, and W. J. Padilla, "Ultra-thin infrared metamaterial detector for multicolor imaging applications," *Opt. Exp.*, vol. 25, no. 19, pp. 23343–23355, 2017.

[41] J. Li, L. Bao, S. Jiang, Q. Guo, D. Xu, B. Xiong, G. Zhang, and F. Yi, "Inverse design of multifunctional plasmonic metamaterial absorbers for infrared polarimetric imaging," *Opt. Exp.*, vol. 27, no. 6, pp. 8375–8386, 2019.

[42] H. Zhu, F. Yi, and E. Cubukcu, "Nanoantenna absorbers for thermal detectors," *IEEE Photon. Technol. Lett.*, vol. 24, no. 14, pp. 1194–1196, Jul. 15, 2012.

[43] S. Ghafari, M. R. Forouzeshfard, and Z. Vafapour, "Thermo optical switching and sensing applications of an infrared metamaterial," *IEEE Sensors J.*, vol. 20, no. 6, pp. 3235–3241, Mar. 2020.

[44] N. Muhammad, Z. Ouyang, X. Tang, and Q. Liu, "Broadband wide-angle incident light absorption by metallic loop metasurfaces based on electro-optic substrate," *IEEE Photon. Technol. Lett.*, vol. 31, no. 13, pp. 1068–1071, Jul. 1, 2019.

[45] F. Yi, H. Zhu, J. C. Reed, A. Y. Zhu, and E. Cubukcu, "Thermoplasmonic membrane-based infrared detector," *IEEE Photon. Technol. Lett.*, vol. 26, no. 2, pp. 202–205, Jan. 15, 2014.

[46] T. Lewi, N. A. Butakov, H. A. Evans, M. W. Knight, P. P. Iyer, D. Higgs, H. Chorsi, J. Trastoy, J. D. V. Granda, I. Valmianski, C. Urban, Y. Kalcheim, P. Y. Wang, P. W. C. Hon, I. K. Schuller, and J. A. Schuller, "Thermally reconfigurable meta-optics," *IEEE Photon. J.*, vol. 11, no. 2, pp. 1–16, Aug. 2019.

[47] B. J. O'Regan, Y. Wang, and T. F. Krauss, "Silicon photonic crystal thermal emitter at near-infrared wavelengths," *Sci. Rep.*, vol. 5, no. 1, pp. 1–8, Oct. 2015.

[48] D. Costantini, A. Lefebvre, A.-L. Coutrot, I. Moldovan-Doyen, J.-P. Hugonin, S. Boutami, F. Marquier, H. Benisty, and J.-J. Greffet, "Plasmonic metasurface for directional and frequency-selective thermal emission," *Phys. Rev. Appl.*, vol. 4, no. 1, pp. 2–7, Jul. 2015.

[49] B. Khalichi, A. Ghobadi, A. K. Osgouei, and E. Ozbay, "Diode like high-contrast asymmetric transmission of linearly polarized waves based on plasmon-tunneling effect coupling to electromagnetic radiation modes," *J. Phys. D, Appl. Phys.*, vol. 54, no. 36, pp. 1–12, 2021.

[50] A. Kong, B. Cai, P. Shi, and X.-C. Yuan, "Ultra-broadband all-dielectric metamaterial thermal emitter for passive radiative cooling," *Opt. Exp.*, vol. 27, no. 21, pp. 30102–30115, 2019.

[51] X. Liu, T. Starr, A. F. Starr, and W. J. Padilla, "Infrared spatial and frequency selective metamaterial with near-unity absorbance," *Phys. Rev. Lett.*, vol. 104, no. 20, pp. 1–4, May 2010.

[52] X. Liu, T. Tyler, T. Starr, A. F. Starr, N. M. Jokerst, and W. J. Padilla, "Taming the blackbody with infrared metamaterials as selective thermal emitters," *Phys. Rev. Lett.*, vol. 107, no. 4, pp. 4–7, Jul. 2011.

[53] D. U. Yildirim, A. Ghobadi, M. C. Soydan, O. Atesal, A. Toprak, M. D. Caliskan, and E. Ozbay, "Disordered and densely packed ITO nanorods as an excellent lithography-free optical solar reflector metasurface," *ACS Photon.*, vol. 6, no. 7, pp. 1812–1822, Jul. 2019.

[54] M. G. Moharam, E. B. Grann, D. A. Pommet, and T. K. Gaylord, "Formulation for stable and efficient implementation of the rigorous coupled-wave analysis of binary gratings," *J. Opt. Soc. Amer. A, Opt. Image Sci.*, vol. 12, no. 5, pp. 1068–1076, 1995.

[55] A. Berk, P. Conforti, R. Kennett, T. Perkins, F. Hawes, and J. Van Den Bosch, "MODTRAN6: A major upgrade of the MODTRAN radiative transfer code," in *Proc. 6th Workshop Hyperspectral Image Signal Process., Evol. Remote Sens. (WHISPERS)*, 2014, pp. 1–4.

[56] V. R. Almeida, Q. Xu, C. A. Barrios, and M. Lipson, "Guiding and confining light in void nanostructure," *Opt. Lett.*, vol. 29, no. 11, pp. 1209–1211, 2004.

[57] H. Kocer, M. C. Cakir, Y. Durna, M. C. Soydan, O. Odabasi, H. Isik, K. Aydin, and E. Ozbay, "Exceptional adaptable MWIR thermal emission for ordinary objects covered with thin VO_2 film," *J. Quant. Spectrosc. Radiat. Transf.*, vol. 262, Mar. 2021, Art. no. 107500.

BAHRAM KHALICHI (Member, IEEE) received the B.Sc. and M.Sc. degrees in electrical engineering from the University of Tabriz, Tabriz, Iran, in 2010 and 2013, respectively, and the Ph.D. degree from Bilkent University, Ankara, Turkey, in 2020. He is currently a Postdoctoral Researcher at the Nanotechnology Research Center, Bilkent University. His research interests include computational electromagnetics, substrate integrated structures, and nanophotonics. He was a recipient of the 2018 Doctoral Research Award from the IEEE Antennas and Propagation Society (AP-S) for his research project on the fast solution of multiscale electromagnetic problems.

AMIR GHOBADI received the B.S. degree in electrical engineering from the University of Tehran, Iran, in 2012, and the M.S. degree from the Department of Electrical Engineering from Bilkent University, Ankara, Turkey, in 2014, where he is currently pursuing the Ph.D. degree. He has published more than 60 articles in SCI journals during his studies, where his articles have received more than 1000 SCI citations with an H-index of 20. His research interests include metasurfaces, nanophotonic structures, infrared sensors, and optoelectronic systems. He is particularly working in the application of lithography-free metadesigns for strong light-matter interaction.

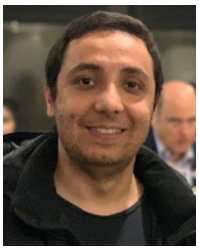

ATAOLLAH KALANTARI OSGOUEI received the B.Sc. degree in physics from Middle East Technical University, Ankara, Turkey, in 2016. He is currently pursuing the M.Sc. degree with the Department of Physics, Bilkent University, Ankara. His research interests include metasurfaces, plasmonics, and nanophotonic structures.

HASAN KOCER received the B.Sc. and M.Sc. degrees from Boğaziçi University, İstanbul, Turkey, in 1995 and 1998, respectively, and the Ph.D. degree from Middle East Technical University, Ankara, Turkey, in 2011, all in electrical and electronics engineering. In 2013, he was a Postdoctoral Fellow with the Metamaterials and Nanophotonic Devices Laboratory, Northwestern University, Evanston, IL, USA. He has been working as a Senior Researcher at the Bilkent University Nanotechnology Research Center (NANOTAM), since September 2019. His current research interests include metamaterials and metasurfaces, nanophotonic structures, GaN-based devices, infrared sensors, thermal radiation, thermal imaging, thermal management, and optoelectronic systems.

EKMEL OZBAY received the M.S. and Ph.D. degrees in electrical engineering from Stanford University, Stanford, CA, USA, in 1989 and 1992, respectively. He held a postdoctoral position at Stanford University. He worked as a Scientist with Iowa State University, Ames, IA, USA. He joined Bilkent University, Ankara, Turkey, in 1995, where he is currently a Full Professor with the Department of Physics and the Department of Electrical and Electronics Engineering. In 2003, he founded the Nanotechnology Research Center (NANOTAM), Bilkent University, where he leads a research group working on nanophotonics, nanometamaterials, nanoelectronics, and GaN-based devices. He is also the CEO of a spin-off company: AB-MicroNano Inc., which was founded to commercialize the technologies developed at NANOTAM. He has published more than 505 articles in SCI journals. His articles have received more than 27 000 SCI citations with an H-index of 80. He was a recipient of the Adolph Lomb Medal of OSA, in 1997, and the European Union Descartes Science Award, in 2005. He has given more than 165 invited talks in international conferences. He served as an Editor for *Optics Letters*, *PNFA*, *JNP* (SPIE), and the IEEE JOURNAL OF QUANTUM ELECTRONICS.